

# Spatial structure in the ACIS OBF contamination

A. Vikhlinin

## Abstract

This memo summarizes the measurements of the spatial and time dependence of the effective contamination optical depth for the L-complex in the ECS spectrum. The developed model results in  $\lesssim 5\%$  uncertainties in the contamination corrections of the effective area at 0.6–0.7 keV and  $< 3\%$  uncertainties at higher energies across both ACIS-S and ACIS-I arrays.

## 1 Introduction

Contamination on the ACIS optical blocking filter is the major calibration problem in analyzing the *Chandra* data. The time, energy, and spatial dependence of the associated X-ray absorption must be measured as accurately as possible. Two types of calibration data are available for the contamination studies, 1) observations of the continuum sources with HETG/LETG+ACIS, and 2) regular exposures to the External Calibration Source. There are also ACIS observations of astronomical “standard candles” which are useful for validation of the contamination model derived from the gratings+ECS data.

The grating data are the best means to establish the chemical composition of the contaminant and its X-ray absorption spectrum, and this has been done (Marshall et al., astro-ph/0308332). However, the grating observations provide very sparse time coverage for only one or two typical locations in ACIS-S. The time dependence and spatial distribution of the contaminant is most accurately derived from the ECS data which provides essentially continuous time coverage for all ACIS CCDs.

As detailed in the ACIS Science Instrument Calibration Report, the ECS spectrum contains a weak Mn+Fe L line near 0.67 keV. It is produced by the same source responsible for the Mn-K $\alpha$  line so the ratio of L and K fluxes should be time-independent. The measured count rate for the L-lines (at  $\langle E \rangle = 0.67$  keV) is sensitive to contamination while that for the Mn-K line at  $E = 5.898$  keV is not. Therefore, any changes in the L/K ratio can be used to derive the effective optical depth of the contaminant at  $E \sim 0.67$  keV as a function of time and position. This measurement is the main goal of our work.

The ECS data and analysis are described in §2. The measurement of the time dependence of the optical depth in several reference regions is presented in §3. The observed spatial pattern of contamination (§4) is consistent with the same functional form which can be normalized using time dependences in the reference regions as described in §4.4. In §5, we describe a procedure which should be used to normalize the contaminant’s absorption spectrum using the ECS-measured optical depth for the time and location of interest. The ECS optical depth at some reference date is the input parameter for the non-uniform contamination model (also known as “fluffium”); this value is provided in §5.2. Finally, in §6, we present the tests of the spatially-dependent contamination model using a series of observations of the galaxy cluster A1795.

## 2 Data and analysis

### 2.1 Data preparation

The main dataset used in the present analysis is the observations of the External Calibration source which are performed regularly during the radiation belt passages. We mostly use the ECS data obtained since January 29, 2000 when the focal plane temperature was lowered to  $-120$  C. Individual ECS observations were extracted from the archive and run through the CTI correction (`acis_process_events`) for the FI chips, if necessary (the CTI correction is already included in the pipeline for the recent observations). The `lev1` event files were then cleaned to the `lev2` state by filtering for ASCA grades 0,2,3,4,6 and removing the standard bad pixels and columns. We consider only I0-I3 and S1, S2, and S3 chips because accurate response calibrations and/or CTI correction is unavailable for the rest.

The event files were split into individual CCDs and then merged into single event files for the 3-month intervals (Feb-Mar-Apr, May-Jun-Jul, Aug-Sep-Oct, and Nov-Dec-Jan). The ACIS gain variations are monitored during the same 3-months (\*\*REF T<sub>GAIN</sub> MEMO\*\*). The observed gain drifts were removed from the merged even file by applying correction to the

photon PI's and energies; simultaneously, we applied the gain table which matches the `calcrmf2` calibration of the ACIS RMFs (it is slightly more accurate than the gain tables in the current CALDB).

There are some bad columns which appear only at low energies (near or below the L-complex) and are left undetected in the standard bad pixel tables. Such columns were detected for each of the 3-months intervals and filtered out from the data.

Finally, we created the response files (ARFs and RMFs) for the spatial regions used in the analysis (32 pixel-wide strips for ACIS-S chips and  $256 \times 256$  pixel squares in ACIS-I). The RMFs were computed with `calcrmf2` (\*\*REF\*\*) and include the latest updates to the response calibration in the FI CCDs<sup>1</sup>. The ARFs include the nominal CCD QE and filter transmission (`acisD1997-04-17qeN0003` version without any recent updates) and the CTI-related QEU correction<sup>2</sup>. For the present analysis, corrections to the average CCD QE are unimportant because the contamination measurement uses the *change* in the observed ratio of the L-complex and Mn-Ka fluxes between in-flight data and ground measurements at the Ball Lab.

### 2.1.1 Data from Fall, 1999

To check that the observed temporal trends in the contamination buildup smoothly point to zero at the time of *Chandra* launch, we used the data obtained in the Fall, 1999 at the focal plane temperature  $-110$  C. The CTI correction and RMFs are not calibrated/implemented for this period and the CTI-induced variations of the quantum efficiency are strong. We therefore, used only the S3 data from the Fall of 1999, and assumed that the calibration of its spectral response (RMFs and ARFs) at  $-120$  C can be used without any modifications.

## 2.2 Spectral model of the L complex and derived optical depth

The spectral model for fitting the ECS spectra is identical to that we used for the Ball measurements<sup>3</sup>. The model of the L-complex in the 0.365–1.1 keV band consists of the following components: (1) Gaussian line with free width at  $E \approx 0.665$  (free) to represent the main peak; (2) Gaussian line at  $E = 0.535$  keV with zero width and the flux 0.0627 that of component 1; (3) power law to model the background continuum; and (4) exponential tail representing the shoulder of the Al-Ka line. There is no strong shoulder of the Al-Ka line in the BI response, therefore the power law with a running spectral index was used to model continuum in the S3 spectra. The main lines in the ECS spectrum are modeled as 5 Gaussians near 1.487 keV (Al-Ka), 4.510 keV (Ti-Ka), 4.930 keV (Ti-Kb), 5.898 keV (Mn-Ka), and 6.486 keV (Mn-Kb). To minimize the influence of imperfections in the RMF model on the flux measurements, we used only the energy range around the main peaks. The representative spectra and the best-fit models are shown in Fig. 1.

Experiments with the choice of the energy range and different versions of the RMFs shows that the Mn-Ka flux is recovered by our spectral fitting with an accuracy of 2% or better. The derived L-flux is rather sensitive to modeling of the underlying continuum. We find that different model and energy band choices typically change the derived flux by 3–5%. Therefore, a systematic uncertainty in the optical depth measurements of  $\Delta\tau = 0.03 - 0.05$  can be expected.

The line fluxes derived from the spectral fit were normalized by the quantum efficiency,

$$f = \frac{\text{Observed flux}}{\text{QE} \times \text{OBF transmission} \times \text{QEU}}, \quad (1)$$

so that the ratio of the L and Mn-Ka fluxes should be position-independent (and ideally, chip-independent) in the absence of OBF contamination. From the analysis of the Ball data, we derived the pre-flight ratios  $f_L/f_{\text{Mn-Ka}}$  for the FI CCDs and S3<sup>4</sup>; using these results, the effective optical depth for the L-complex is obtained from the ratio of normalized fluxes as

$$\begin{aligned} \tau_L &= -4.687 - \log(f_L/f_{\text{Mn-Ka}}) && \text{for S3} \\ \tau_L &= -4.925 - \log(f_L/f_{\text{Mn-Ka}}) && \text{for ACIS-I and S2} \end{aligned} \quad (2)$$

## 3 Time dependence

We demonstrate below (§4) that the spatial pattern of the contamination in both ACIS-I and ACIS-S is described by the same functional form,  $\tau = \tau_0 + \tau_1 r^a$  where  $r$  is the distance from a reference region in each array. Within the measurement uncer-

<sup>1</sup><http://hea-www.harvard.edu/~alexey/acis/memos/rmfupdate.pdf>

<sup>2</sup><http://hea-www.harvard.edu/~alexey/acis/memos/qeu.pdf>

<sup>3</sup><http://hea-www.harvard.edu/~alexey/acis/memos/balldata.pdf>

<sup>4</sup><http://hea-www.harvard.edu/~alexey/acis/memos/balldata.pdf>

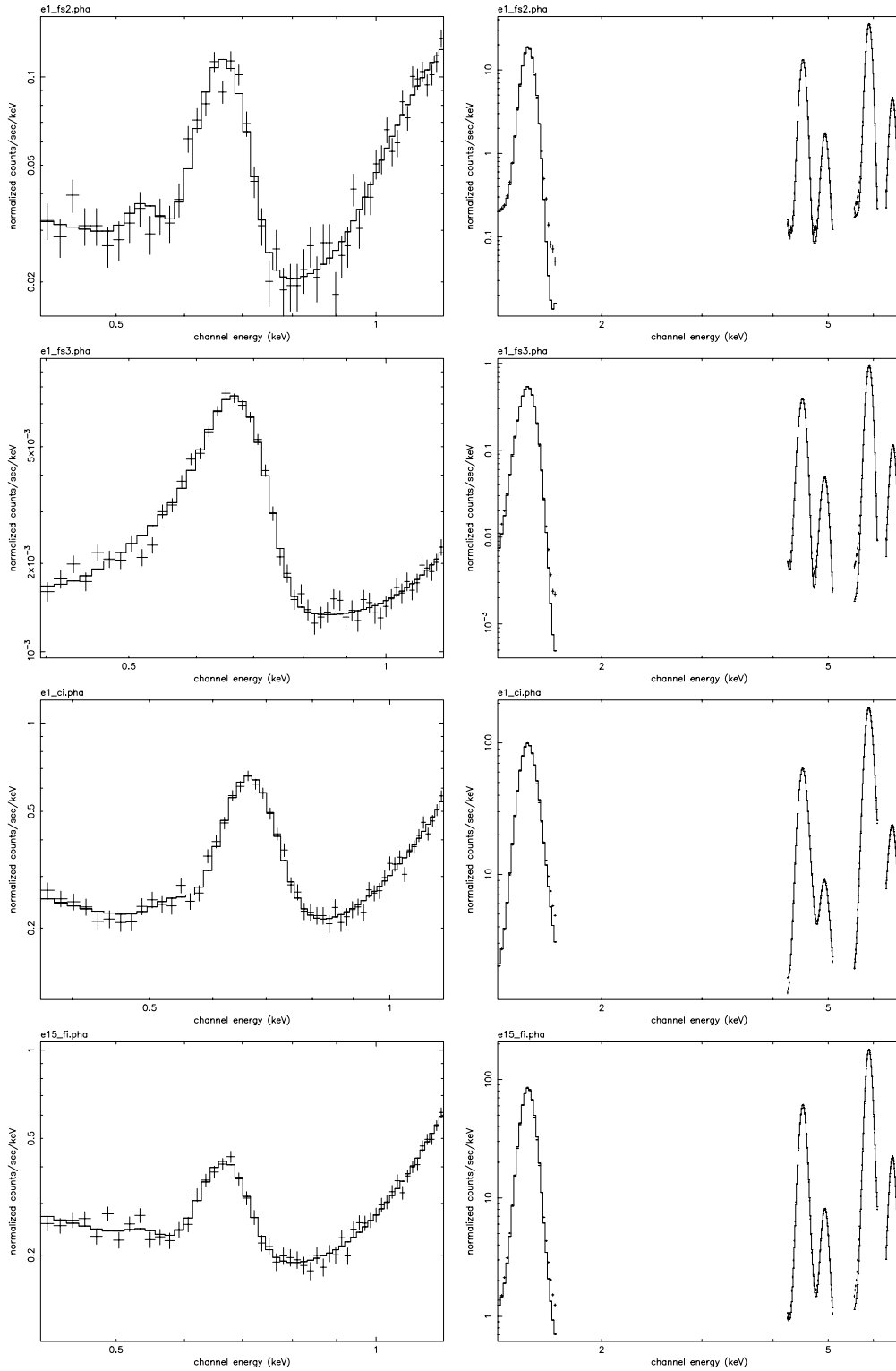


Fig. 1— Representative sample of the observed ECS spectra and the best-fit models.

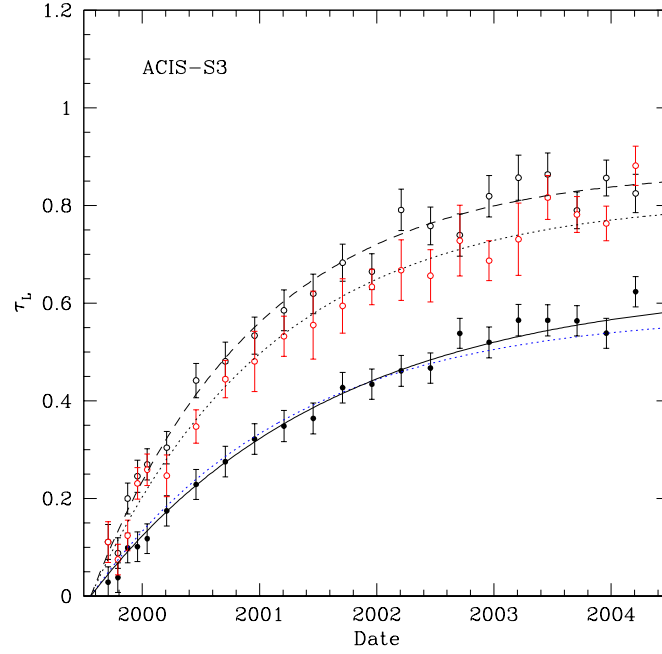


Fig. 2— Time dependence of the L-complex optical depth in S3. The filled circles show the measurements at the center of ACIS-S3 (region cs) and the solid line is the fit by eq. (3). The open circles are the measurements near the readout of S3 (black, region bs) and at the top of S3 (red, region ts); the fit of eq. (4, 5) is shown by the dashed line. The dotted line shows the model suggested by A. Tennant at the end of 2002.

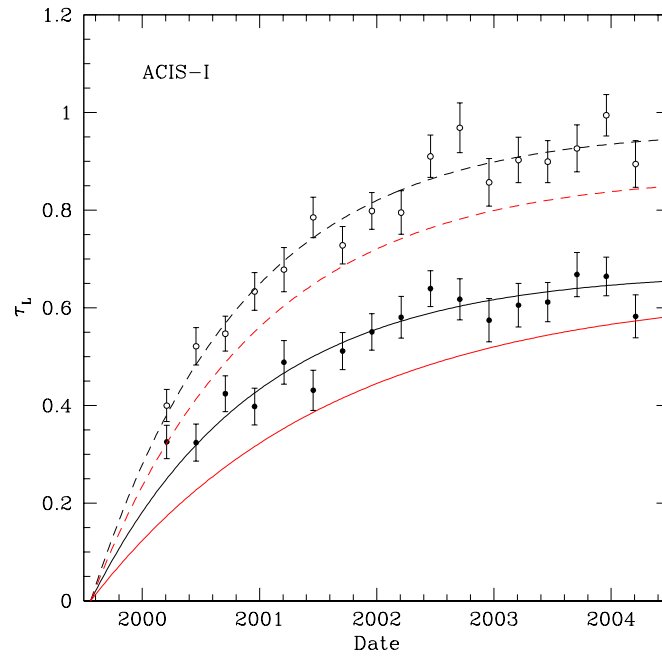


Fig. 3— Time dependence of the L-complex optical depth in ACIS-I. The filled and open circles show the measurements at the center and border of the ACIS-I, respectively (regions ci and fi). The black solid and dashed lines show the fits by eq. (6) and (7). Red lines show the corresponding fits to the ACIS-S data.

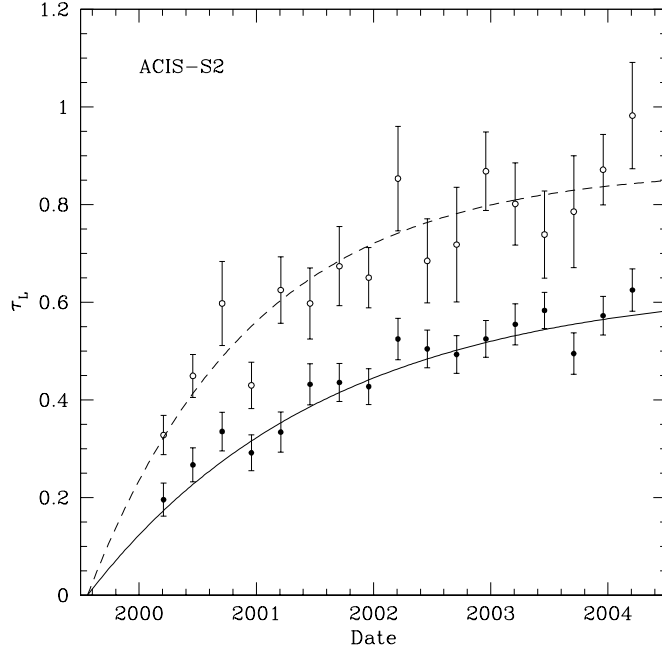


Fig. 4— Contamination time dependence measured with the S2 data. The filled circles show the data for the center of the chip (the region identical to cs and the open circles are for the bottom of the chip (identical to bs). The red lines are the fits to the S3 data in the corresponding regions.

tainties, the indices  $a$  are time-independent and only  $\tau_0$  and  $\tau_1$  experience a gradual increase. Therefore the spatial pattern can be normalized by the observed time evolution in reference regions in each array, one at the center and the others near the edge where the contamination is maximal. We use the following regions:

- ci — Center of the I array. Defined as a square  $1024 \times 1024$  CCD pixels around the center of the I array (the gap between the ACIS-I CCDs is ignored).
- fi — Edge of the I array, defined as a frame with the width 256 CCD pixels along the ACIS-I border.
- cs — Center of S3, CHIPY = 256 – 768.
- bs — Bottom of S3, CHIPY = 8 – 128.
- ts — Bottom of S3, CHIPY = 897 – 1023.

The measurements are shown in Fig. 2 and 3. Clearly, the rate of the contamination buildup gradually decreases in each region. The time dependence,  $\tau(t)$ , can be fit with the exponential saturation model suggested by A. Tennant:

$$\tau_{cs}(t) = 0.63997 \times [1 - \exp(-t/2.0541)] \quad (3)$$

$$\tau_{bs}(t) = 0.87532 \times [1 - \exp(-t/1.4093)] \quad (4)$$

$$\tau_{ts}(t) = 0.81544 \times [1 - \exp(-t/1.5362)] \quad (5)$$

$$\tau_{ci}(t) = 0.67499 \times [1 - \exp(-t/1.4042)] \quad (6)$$

$$\tau_{fi}(t) = 0.96650 \times [1 - \exp(-t/1.2951)] \quad (7)$$

where  $t$  is the time since *Chandra* launch in years ( $t_{\text{launch}} = 1999.56$ ). These fits are shown in Fig. 2–3. In Fig. 2, we also show the Tennant’s fit to independent measurements of the average optical depth in S3 over 1999–2002 provided by C. Grant. Our fit is very close to that model.

Note that we find slightly higher contamination at the center of ACIS-I relative to ACIS-S,  $\Delta\tau = 0.08$ . This is somewhat counter-intuitive because the center of the I-filter is expected to be warmer (Fig. 5) yet the ECS measurement is supported by observations of astrophysical sources, see §6. It might be suggested that some errors in the cross-calibration of the FI and BI CCDs could contribute to the inferred contamination differences. However, we find that the contamination measured from the S2 data (FI chip) is identical to the S3 results (Fig. 4).

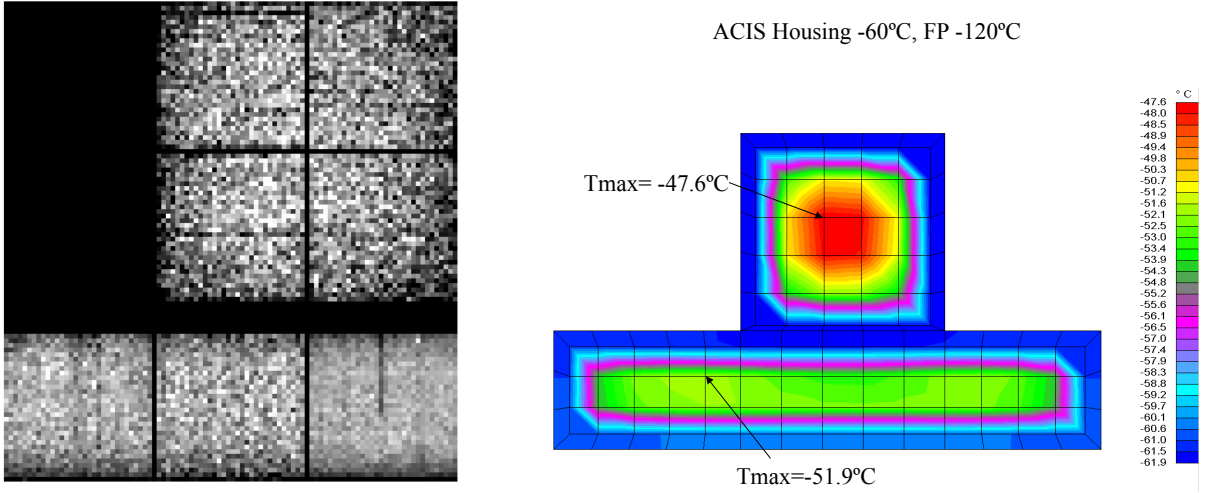


Fig. 5— *Left*: Distribution of the observed flux of the L-complex in the ECS spectrum ( $E = 0.53 - 0.80$  keV) in ACIS-I and S1, S2, and S3. The intensities has been normalized to the values in the centers of each array. The observed variations are much greater than those expected from the CTI-related quantum efficiency variations or the illumination pattern for the Mn lines. The spatial structure is mostly due to contamination of the OBF; it is qualitatively consistent with the expected temperature distribution on the OBF (*Right*; this panel shows the model for the temperature distribution on the ACIS OBF provided by N. Tice).

## 4 Spatial dependence

### 4.1 General considerations

A general picture of the spatial pattern of the ACIS contamination can be obtained from the observed distribution of the ECS flux in the L-complex energy range. The combined image (August, 2000 — December, 2003) in the 0.53–0.8 keV energy band is shown in Fig. 5. It is clear that the contamination is non-uniform; *in ACIS-I, the pattern is circularly symmetric around the center of the array; in ACIS-S, the pattern depends only on the Z coordinate (CHIPY)*. This is qualitatively consistent with the expected temperature distribution on the OBF (right panel of Fig. 5) and the expectation that the colder parts of the OBF accumulate more contaminant. More careful analyses show no statistically significant deviations from these patterns (i.e., no azimuthal variations in ACIS-I and CHIPY variations in ACIS-S). In what follows, we consider the distribution of the contaminant only as a function of off-center distance in ACIS-I and CHIPY in ACIS-S. Detailed measurements of the spatial pattern of the contamination in both arrays is obtained from the distribution of the L/K flux ratio in the data averaged over 1-year intervals starting from February, 2000.

### 4.2 ACIS-S

Since the distribution of the contaminant on the S-filter is one-dimensional (a function of CHIPY only), we determine its pattern from fitting the S3 spectra extracted in narrow strips,  $\Delta\text{CHIPY} = 32$ , spanning all 4 nodes of the S3 CCD. It has been verified that consistent results are obtained from fitting the S2 spectra (see Fig. 4), but the accuracy in this case is poorer because of the lower quantum efficiency.

The measurements at 4 epochs are presented in Fig. 6. As the contamination builds up, it becomes progressively non-uniform. Fortunately, the observed pattern can be fit with a function of the same type at all epochs

$$\tau(y) = \begin{cases} \tau_0 + \tau_1 |y - 512|^{5.5} & \text{for } y < 512 \\ \tau_0 + \tau_2 |y - 512|^{4.5} & \text{for } y > 512 \end{cases} \quad (8)$$

where only normalizations  $\tau_0$  and  $\tau_{1,2}$  are time-dependent. The fits with this function are shown by solid lines in Fig 6.

As a consistency check, we have measured the contamination from the Ball Lab dataset. As expected, the ground-based data shows no trends in the L/K ratio within the statistical accuracy (Fig. 7).

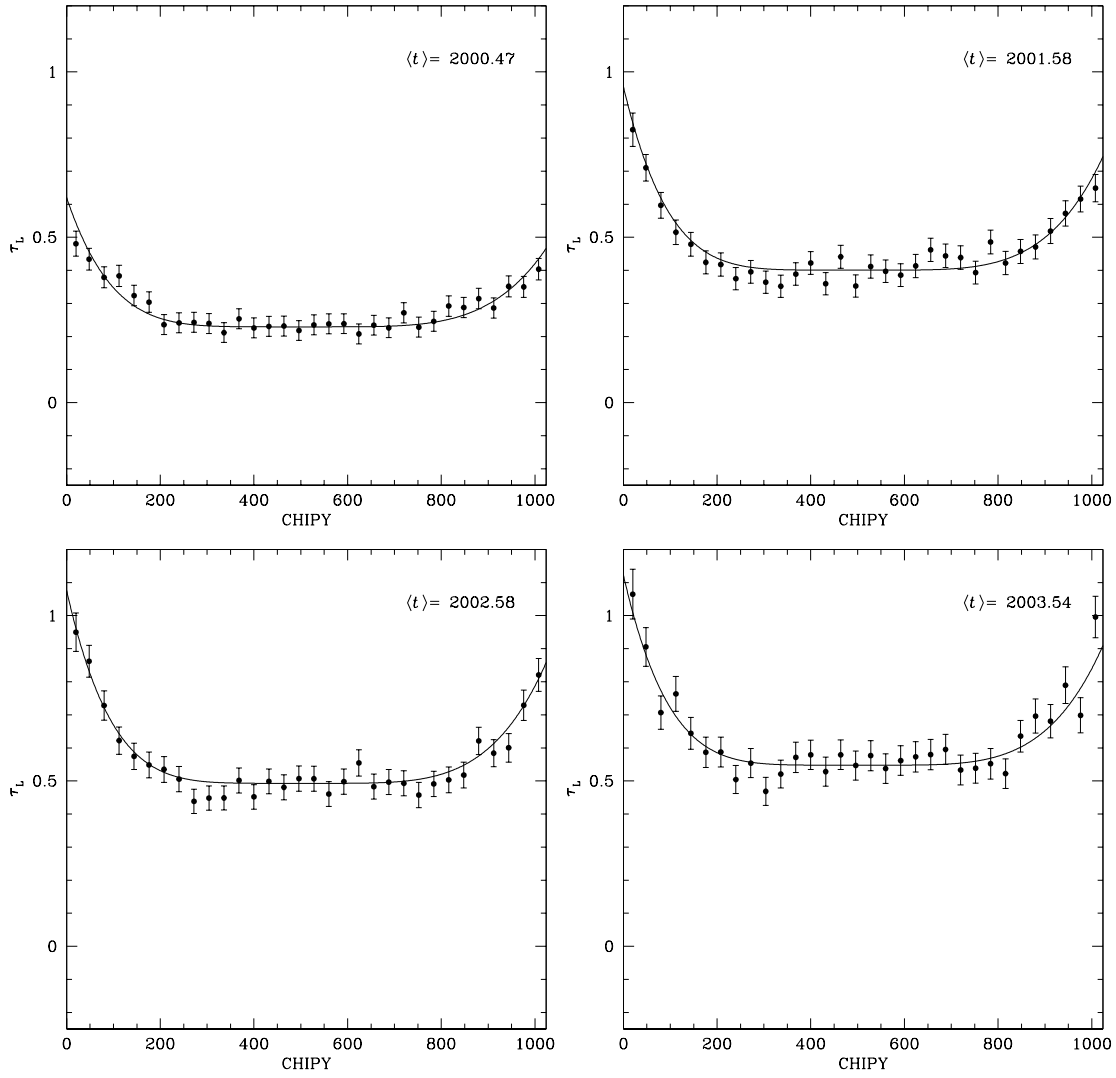


Fig. 6— Optical depth of the L-complex as a function of CHIPY in S3 at 1 year intervals starting in February, 2000. Solid lines show the fit from equation (8) normalized using the time dependences in eq. (3)–(4) assuming that the cs region is at CHIPY = 512, bs is at CHIPY = 64, and  $\tau_S$  is at CHIPY = 964.

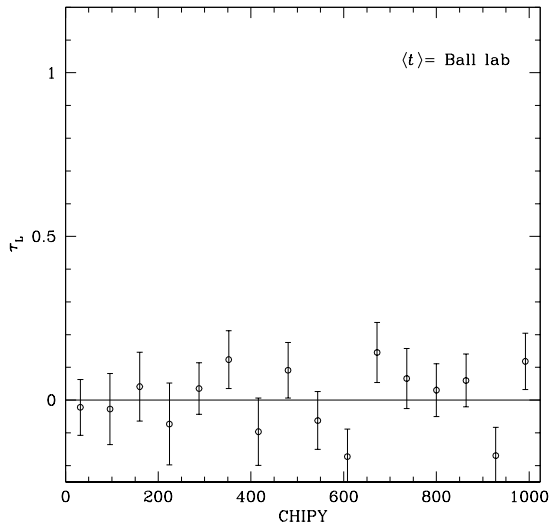


Fig. 7— Same as Fig. 6 but for the Ball Lab dataset. No contamination is expected at that time and the  $L/K$  ratio is indeed uniform within the statistical accuracy

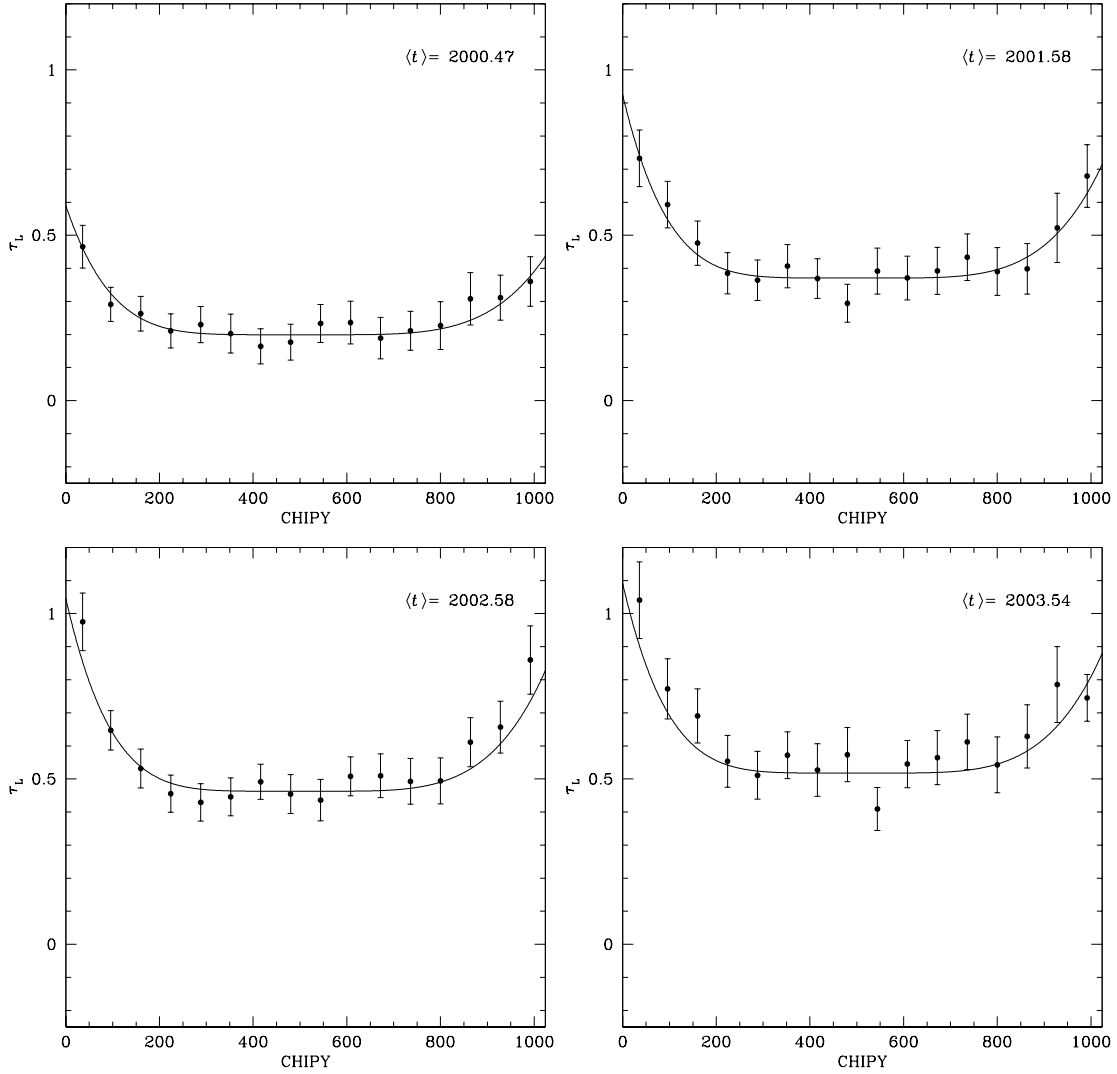


Fig. 8—Optical depth of the L-complex as a function of CHIPY in the S1 chip. Solid lines show the fits to the S3 data from Fig. 6.

#### 4.2.1 Are S1 and S3 contaminations the same?

The identical analysis of the contamination in S1 shows that both its time dependence and spatial distribution can be described by the S3-derived model as shown in Fig. 8. Note that the low-energy edge structure of the contaminant is derived from the grating measurements strictly speaking, for the S1 chip. Our results indicate that the S1 measurements can be used for S3.

### 4.3 ACIS-I

The azimuthally-averaged profiles of the contamination optical depth in ACIS-I at 4 epochs are shown in Fig. 9. They also can be fit with the const + power law function with the fixed power law index and time-dependent normalizations (solid lines in Fig. 9):

$$\tau(r) = \tau_0 + \tau_1 r^\gamma, \quad \gamma = 2.0. \quad (9)$$

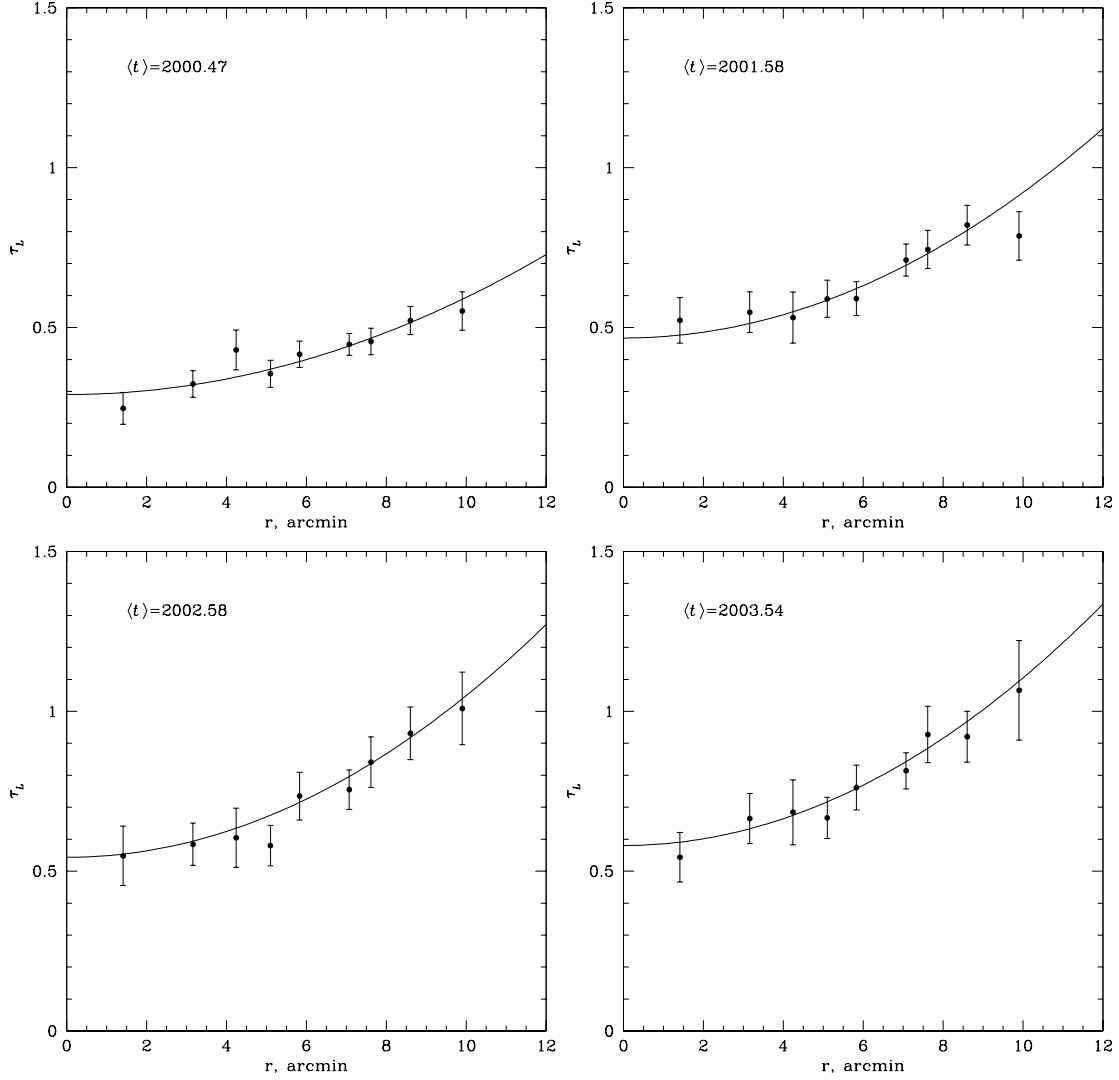


Fig. 9— Optical depth of the L-complex as a function radius from the center of ACIS-I averaged over 1-year intervals starting in February, 2000. Solid lines show the fit from equation (9) the time dependences in eq. (6)–(7) as explained in §4.4.3.

#### 4.4 How to normalize the spatial patterns

##### 4.4.1 Flux-weighted locations

The time-dependence of the contamination is derived from the spatial regions of finite size. The flux-weighted location within those regions must be used for normalization of the spatial pattern. The flux-weighted coordinate is determined as follows. The average line flux in a region where contamination changes as  $\tau = \tau_0 + \tau_1^y$  is

$$\bar{f} = \frac{1}{S} \iint \exp(-\tau_1 r^y) dx dy, \quad (10)$$

where  $S$  is the area of the region. The average optical depth is then

$$\bar{\tau} = -\log(\bar{f}) = -\log\left(\frac{1}{S} \iint \exp(-\tau_1 r^y) dx dy\right), \quad (11)$$

and the average location is

$$\bar{r} = (\bar{\tau}/\tau_1)^{1/y} \quad (12)$$

#### 4.4.2 ACIS-S

The contamination pattern in ACIS-S deviates from the constant value only in narrow regions near the readout and at the top of the CCD. Therefore,  $\tau_{cs}$  directly gives  $\tau_0$  in eq. (8). The  $\tau_{1,2}$  terms can be found from the difference between  $\tau_{bs,rs}$  and  $\tau_{cs}$ . The flux-weighted average  $y$ -coordinate in the bs region is CHIPY = 64. Therefore,

$$\tau_{bs} = \tau_0 + \tau_1 |64 - y_0|^{\alpha_1} = \tau_{cs} + \tau_1 |64 - y_0|^{\alpha_1} \quad (13)$$

$$\tau_1 = (\tau_{bs} - \tau_{cs}) \times |64 - y_0|^{-\alpha_1} \quad (14)$$

and finally,

$$\tau(y) = \tau_{cs} + (\tau_{bs} - \tau_{cs}) \times \left| \frac{y - y_0}{64 - y_0} \right|^{\alpha_1}, \quad (15)$$

where all  $y$ 's are in CCD pixels and the  $y_0$  and  $\alpha$  parameters are given in eq. (8). The flux-weighted average  $y$  in the rs region is 964, therefore for CHIPY > 512 the contamination pattern is normalized as

$$\tau(y) = \tau_{cs} + (\tau_{rs} - \tau_{cs}) \times \left| \frac{y - y_0}{964 - y_0} \right|^{\alpha_2}, \quad (16)$$

#### 4.4.3 ACIS-I

Using eq. (10–12) we find the average radii **3.24' = 415 CCD pixels for cr<sup>5</sup>** and **8.07' = 1033 pix for FI** for  $\gamma = 2$ , virtually independent of  $\tau_1$  in a reasonable range of values. Therefore, the spatial pattern in ACIS-I can be normalized as follows,

$$\begin{aligned} \tau_{ci} &= \tau_0 + \tau_1 \times 3.24^\gamma \\ \tau_{fi} &= \tau_0 + \tau_1 \times 8.07^\gamma, \end{aligned} \quad (17)$$

$$\begin{aligned} \tau_1 &= \frac{\tau_{fi} - \tau_{ci}}{8.07^\gamma - 3.24^\gamma} \\ \tau_0 &= \tau_{ci} - 3.24^\gamma \times \frac{\tau_{fi} - \tau_{ci}}{8.07^\gamma - 3.24^\gamma}, \end{aligned} \quad (18)$$

and finally,

$$\tau(r) = \tau_{ci} + \frac{\tau_{fi} - \tau_{ci}}{8.07^\gamma - 3.24^\gamma} (r^\gamma - 3.24^\gamma), \quad (19)$$

where  $r$  is in arcmin and  $\gamma$  is given in eq. (9). The profiles of  $\tau$  calculated using this equation are shown by the solid lines in Fig. 9.

## 5 How to go from $\tau_L$ to $\tau(E)$ ?

Using the results of §4.4, we can compute the effective optical depth for the L-complex at any location. We need to know the optical depth at all energies for the proper spectral analysis. The best we can do at present is to assume that the chemical structure of the contaminant is constant (only thickness varies) and renormalize the absorption spectrum accurately measured from the grating observations at a single location (Marshall et al., astro-ph/0308332). The renormalization procedure is described below.

### 5.1 How to normalize the standard contamination spectrum?

The L-complex consists of several lines with the energies  $E_i$ ; let  $c_i$  be their observed count rates before contamination. The absorption coefficient can be written as  $a(E) = \exp(-A \times \tau(E))$ , where  $\tau(E)$  is the “standard” contamination spectrum provided by the grating measurements and  $A$  is the normalization constant we want to find. The observed flux in the L-complex is

$$C = \sum c_i \times a(E_i) = \sum c_i \times \exp(-A \tau(E_i)). \quad (20)$$

<sup>5</sup>We convert CCD pixels to arcmin assuming that 1024 pix = 8' and there are no gaps between the chips

Table 1— Inferred composition of the ECS L-complex

| Line group               | $E$ , keV | $f(\text{FI})$ | $f(\text{BI})$ |
|--------------------------|-----------|----------------|----------------|
| Fe $\alpha, \beta$ ..... | 0.706     | 39%            | 33%            |
| Mn $\alpha, \beta$ ..... | 0.638     | 54%            | 58%            |
| Fe $\zeta, \eta$ .....   | 0.618     | 2%             | 3%             |
| Mn $\zeta, \eta$ .....   | 0.559     | 5%             | 6%             |
| <i>Empirical fit</i>     |           |                |                |
| X $\alpha$ .....         | 0.665     | 93%            |                |
| X $\zeta$ .....          | 0.535     | 7%             |                |

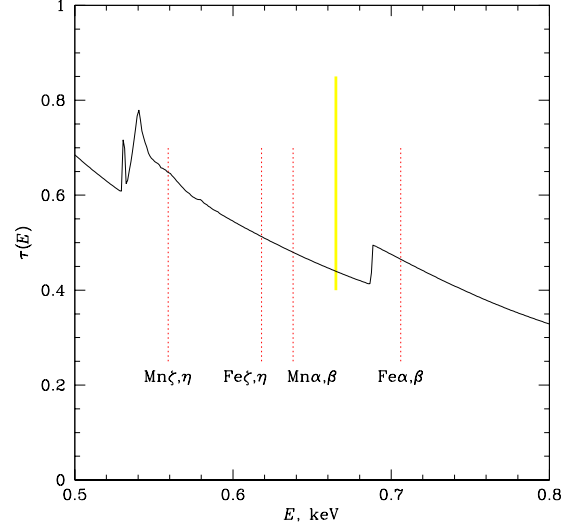


Fig. 10— The absorption spectrum of the ACIS contaminant derived from the grating analysis and the expected locations of the ECS L-complex lines. The yellow line indicates the empirical location of the single broadened line.

Therefore, the effective optical depth derived from the L-to-Mn-K $\alpha$  analysis is

$$\exp(-\tau_L) = \frac{C}{\sum c_i} = \sum f_i \times \exp(-A \tau(E_i)) \quad (21)$$

where  $f_i$  is the count rate fraction for the  $i$ -th line before contamination. If all  $\tau(E_i)$  are close (as expected if  $E_i$  are close), eq. (21) can be linearized and solved with respect to  $A$ ,

$$A = \frac{\tau_L}{\sum f_i \tau(E_i)}. \quad (22)$$

This answer is obviously valid also for a single isolated line.

Equation (22) can be used for normalization of the absorption spectra at each location (where  $\tau_L$  is obtained as described in §4.4), if the energies and locations of the L-complex components are known. We expect that the L-complex contains a mixture of emission lines from Fe and Mn and the nominal locations of these lines are known. Therefore, the count rate fractions can be established from the observed average energy of the L complex. The results of this analysis<sup>6</sup> are summarized in Table 1 and the line locations are indicated in Fig. 10.

Important caveat is that the pre-flight spectrum of the L-complex in the FI CCDs is better fit by a single slightly broadened ( $\sigma = 27$  eV) line at 0.665 keV and a weak line at 0.535 keV than by the mixture of Fe and Mn  $\alpha+\beta$  lines at the expected locations. The practical difference between these two structures of the L-complex is characterized by the flux-weighted optical depth in the denominator of eq. (22). For the actual absorption spectrum shown in Fig. 10 (it corresponds to the 2003 contamination), we find  $\sum f_i \tau_i = 0.492$  for the lines at the standard locations, and 0.475 for the empirical two lines fit. The difference between these two cases is 4% in terms of the optical depth and 1.7% in terms of the effective area at 0.6–0.7 keV. Given the small difference, *we recommend using the physically-motivated model with lines at the standard locations.*

## 5.2 Input to “fluffium”

There is some difference between the measurement of the contamination optical depth at L-shell using the external calibration source and the gratings data. The difference can be reconciled if contamination is spatially non-uniform<sup>7</sup>. The non-uniform model is commonly referred to as “fluffium”.

<sup>6</sup><http://hea-www.harvard.edu/~alexey/acis/memos/balldata.pdf>

<sup>7</sup>See Dan Dewey’s notes <http://space.mit.edu/HETG/technotes/contam/twolevel.html>. The basic idea is that the grating data accurately measures the optical depth just above the C-K, O-K, and F-K edge energies, which are then extrapolated to 0.67 keV; the extrapolation is different for spatially uniform and non-uniform contamination

Table 2— Log of A1795 observations

| OBSID     | Date       | ACIS Location            |
|-----------|------------|--------------------------|
| 494.....  | 1999-12-20 | S3, CHIPX=376, CHIPY=512 |
| 493.....  | 2000-03-21 | S3, CHIPX=376, CHIPY=512 |
| 3666..... | 2002-06-10 | S3, CHIPX=376, CHIPY=512 |
| 5286..... | 2004-01-14 | S3, CHIPX=376, CHIPY=90  |
| 5287..... | 2004-01-14 | S3, CHIPX=376, CHIPY=512 |
| 5288..... | 2004-01-16 | S3, CHIPX=376, CHIPY=908 |
| 5289..... | 2004-01-18 | I3, CHIPX=808, CHIPY=844 |
| 5290..... | 2004-01-23 | I3, CHIPX=136, CHIPY=160 |

The experimental input to the fluffium model is the edge depths derived from the LETG observation of Mkn421 at  $t = 2002.82$  and the optical depth for the L-complex derived from the ECS data for the same date. The source was placed at  $\text{CHIPY} = 177$ . Our spatially-dependent model gives  $\tau_L = \mathbf{0.564}$  for this date and location. This is the effective optical depth for the mixture of spectral lines given in Table 1,

$$\exp(-\tau_L) = 0.33 \exp(-\tau(0.706)) + 0.58 \exp(-\tau(0.638)) + 0.03 \exp(-\tau(0.618)) + 0.06 \exp(-\tau(0.559)) \quad (23)$$

Our value is above the L-complex optical depth 0.46 used in the original fluffium model. The difference is mostly due to the spatial dependence of the contamination neglected previously. \*\*\*THE FLUFFIUM MODEL MUST BE REVISED USING THE NEW VALUE FOR  $\tau_L$ \*\*\*.

## 6 Tests with Abell 1795

The nearby bright galaxy cluster A1795 was observed 8 times during the Chandra mission (Table 2). This is a bright source with quasi-continuum spectrum extending down to 0.4 keV. Although A1795 has a high total count rate, it is not piled-up because the cluster emission is extended with a typical size of  $\sim 2'$ .

Observations of A1795 can be used to test both the time dependence and the spatial dependence of the ACIS contamination:

- OBSIDs 494, 493, 3666, and 5287 were made at the identical location on the S3 chip over the time period 12/1999–01/2004. These data test the time dependence at the center of S3.
- OBSIDs 5286, 5287, and 5288 were made within 2 days of each other at different CHIPY's on the S3 chip. These data test the spatial pattern of contamination on the S filter.
- OBSID 5289 near the ACIS-I aimpoint was made just after the 528\* series of S3 observations. Comparison of these data (and also 494, 493, and 3666) gives the cross-calibration between S3 and I3, including the difference in contamination at the centers of the ACIS-I and ACIS-S arrays.
- The comparison of OBSID 5289 and 5290 can be used to verify the spatial dependence of contamination in ACIS-I.

The following approach was used for the data analysis. First, we identified the optimal spectral extraction region for each of the tests. The regions are defined in the sky coordinates excluding the chip boundaries and bad CCD columns (convolved with the aspect histogram) from each of the pointings of interest so that the physical flux from each of the regions must be identical. We used only the central part of the cluster (within  $2'$  of the center) where the object brightness is much higher than the background.

We then extracted the cluster spectra and generated response data and the background from the blank-field datasets. It was verified that the background subtraction has a negligible effect (variations of the background normalization by 50% changed the measured flux by less than 1%). The response files (ARFs and RMFs) were flux-weighted over the region of interest. The RMFs were computed using `CALCRMF2` with all latest updates. The ARFs were computed using `CALCARF` including

1. The CCD + filter QE with the recent MIT fixes for the BI chips at low energies.
2. The new QEU model based on the Mn-Ka data and the grade fraction as a function of energy, see <http://hea-www.harvard.edu/~alexey/acis/memos/qeu.pdf>
3. Updated S3 QE at  $E > 3$  keV. This fix does not affect the contamination analysis.

The QE model we used has a depth of the depletion layer of  $46\mu$  instead of  $39\mu$  in the current CALDB file. The motivation for this fix is that the depletion depth was adjusted to the ground calibration data averaged over the chip. The flux loss at high energies caused by the CTI-induced QUE is approximately equivalent to underestimation of the depletion depth by  $7\mu$ .

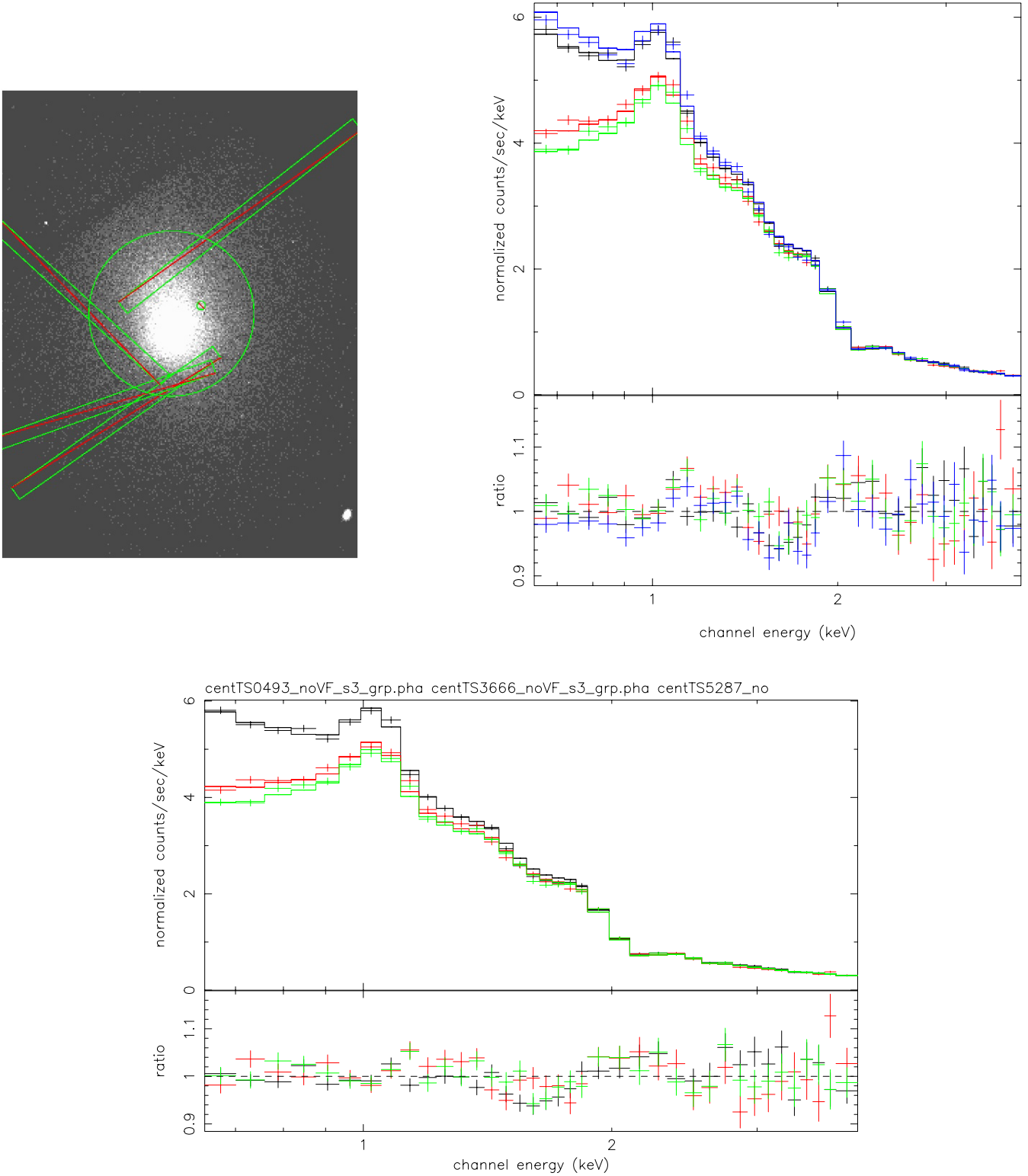


Fig. 11— Test of the **time dependence at the center of S3** using A1795 observations with OBSID 494, 493, 3666, and 5287. The spectral extraction region is shown in the top-left panel. The simultaneous fit to all 4 OBSIDs is shown in top-right (blue, black, red, green for OBSID 494, 493, 3666, and 5287, respectively). Notice the factor of 1.5 drop in the count rate at  $E = 0.6$  keV caused by the contamination buildup, included in the ARF model. The bottom panel shows the joint fit to the  $T = -120$  C data only (OBSID 493, 3666, and 5287).

4. The fix to the HRMA effective area which corresponds to the 7 Å hydro-carbon film on the mirror surface. This fix does not affect our relative QE tests because it was applied identically to all OBSIDs but it helps to reduce  $\chi^2$  for the best-fit models.

The possible HRMA contamination was discussed at the 2003 Chandra calibration workshop, see <http://cxc.harvard.edu/ccw/proceedings/index.html/presentations/marshall12/index.html>

We used the HRMA area model with the 10 Å contamination provided by D. Jerius, and scaled the difference between the 10 Å and 0 Å layers by a factor of 0.7 to obtain the correction corresponding to the 7 Å film. 7 Å is the best-fit value for our combined A1795 spectra.

5. *Most importantly*, CALCFIT implements the spatially-dependent contamination model presented in this document. The contamination absorption spectrum was taken from the “fluffium” model (aciSD1999-08-13contamN0003). It was rescaled using the ECS-derived  $\tau_L$  for the given location and date using the procedure described in §5.

As explained in §5.2, the fluffium spectrum needs to be updated. However, the difference between various contamination models is very small above 0.6 keV if they are scaled to the same optical depth at the L-complex energies. Therefore, some residuals between the data and the best-fit model can be expected below 0.6 keV but our tests should be reliable at higher energies.

To check the validity of the contamination model with the A1795 data, we verify that for each of the tests outlined above, the spectra in the identical regions from the different OBSIDs can be fit simultaneously with the same physically-motivated spectral model, including normalization. The X-ray flux from the central region of A1795 is expected to be due to the optically thermal plasma emission with a range of temperatures. We therefore used the two-component VMEKAL model with the free temperatures and normalizations of each component and the metal abundances tied between the two. The overall spectrum was modified by the Galactic absorption with  $N_H = 1.19 \times 10^{20} \text{ cm}^{-2}$ .

### 6.1 Time dependence at the center of ACIS-S: OBSIDs 494, 493, 3666, and 5287

To check the contamination time dependence at the center of S3 we used the spectra from OBSIDs 494, 493, 3666, and 5287 extracted in the 2' circle around the cluster center excluding the regions falling on bad columns in either of the pointing and also a variable point source 0.7' to the North-West of the cluster center; the extraction region is shown in the top-left panel of Fig. 11. The joint fit to all 4 datasets is shown in the top-right panel of Fig. 11. Note that the physical model — including normalization — is the same for all OBSIDs. The gradual decrease of the count rate at low energies is due to the contamination buildup. Its is properly included in the ARF model as manifested by small residuals from the fit. *Even though the effective area at 0.6 keV decreases by a factor of 1.5, we are able to fit the spectra simultaneously to within a 5% accuracy.*

The strongest residuals are at the right wing of the emission line complex at  $\sim 1$  keV (this is related to inaccuracies in the the physical model of the source spectrum) and around 1.8 keV probably due to imperfect RMF model in the BI CCDs just above the Si K-edge. In fact, a closer examination shows that the strongest residuals are for OBSID 494, which was performed in December, 1999 at the focal plane temperature  $-110$  C. We assumed that the calibration of the BI CCD (gain, RMF) at this temperature is identical to that for  $T = -120$  C in the Spring of 2000, but this may be only the zero-order approximation. If OBSID 494 is removed, the residuals in the joint fit become even smaller,  $\sim 3\%$  (bottom panel of Fig. 11).

### 6.2 Spatial dependence in ACIS-S: OBSIDs 493, 3666, 5287, and 5286 + 5288

To test the contamination spatial structure in ACIS-S, we used OBSIDs 5286, 5287, and 5288 in which the cluster center was placed at the bottom, in the center, and at the top of the S3 chip, respectively (Fig. 12). The spectra were extracted in the 80'' strips and within 2' of the cluster center. The strips were aligned with the chip boundaries in OBSIDs 5286 and 5288. There is a bright filament of the cold gas near the cluster center and its spectrum is very different from the rest of the cluster. This filament is attenuated differently at the center and near the edges of S3 so the spectra from these locations are hard to compare directly. We, therefore, excluded the filament from the extraction region for this test (small ellipses in the top panel of Fig. 12). The spectral variations in the rest of the cluster are small and so different locations can be compared directly.

The reference fit was obtained using the data from OBSIDs 493, 3666, and 5287 in which the cluster was located at the center of S3. As in the previous test, the joint fit is good despite a strong (but properly modeled) time-dependence of the contamination (bottom-left panel in Fig. 12). We then applied the best-fit reference model to the 528\* series (bottom-right panel in Fig. 12). There is a clear drop of the effective area at low energies both at the top and at the bottom of S3. Its is

accurately included in the ARF model as illustrated by the small residuals from the reference fit which do not exceed 5% at all energies of interest, including Poisson noise.

### 6.3 Cross-calibration between the centers of ACIS-S and ACIS-I: OBSIDs 493, 3666, 5287, and 5289

The cross-check between the centers of ACIS-I and ACIS-S was performed with the data from OBSIDs 493, 3666, 5287, and 5289. The spectra were extracted in the  $2.6' \times 2.6'$  box aligned with the chip boundaries in the ACIS-I pointing (Fig. 13). The reference model was obtained by fitting the data for the 3 ACIS-S OBSIDs (left panel in Fig. 14).

The best-fit reference model applied to the ACIS-I spectrum reveals systematic negative deviations of the data (middle panel in Fig. 14). This is expected since the cosmic ray plumes produce a “dead area” effect in the FI chips (\*\*REF TO YOUSAF’S MEMO\*\*). In a typical 3.4 s frame,  $\sim 4\%$  of the CCD area is lost to the cosmic rays. By fitting the energy-independent normalization factor of the reference model to the OBSID 5289 data, we find that a correction of  $(3.6 \pm 0.4)\%$  is required, consistent with the expected dead area effect. After this *energy-independent* correction is applied to the reference model, the ACIS-I residuals are within 3–5% throughout the energy range (right panel in Fig. 14).

### 6.4 Spatial dependence in ACIS-I: OBSIDs 5289 and 5290

Finally, we can test the contamination spatial dependence in ACIS-I using the data from OBSIDs 5289 and 5290. The cluster center was placed in the I3 chip in both cases. 5289 was done near the ACIS-I aim point where the contamination is minimal. In 5290, the cluster was placed at the corner of ACIS-I where the optical depth at 0.67 keV is larger by 0.4 according to the ECS data (Fig. 9); the difference should be easily detectable.

The comparison of the spectra between these two pointings relies on the correct calibration of the HRMA vignetting. Note that the SIMZ offset was applied in both OBSIDs to put the cluster as close to the optical axis as possible. The difference in the off-axis angles in these two cases is  $6'$  and the corresponding vignetting correction at low energies is only  $\sim 7\%$ , much smaller than the expected effect of the contamination.

The spectral extraction regions are shown in Fig. 15 and the observed spectra in Fig. 16. As expected, there is a string difference in the observed count rates at low energies, most of which is included in the ARF model.

Note that when the model normalizations for the two OBSIDs are forced to be equal, there is a small but noticeable difference in the residuals so that the observed flux in OBSID 5290 is slightly higher. The observed difference could be explained by the CHIPY-dependence of the dead area effect. Since the cosmic rays hit the readout frame as well as the imaging area, the *dead area near the readout is expected to be a factor of 2 smaller than that at the top of the CCD*. We estimated the 3.6% dead area correction at the top of I3 from the ACIS-S vs I cross-check (§6.3); therefore, one could expect a 1.8% difference in the normalizations between OBSIDs 5290 and 5289. When this correction is done, the agreement between the observed fluxes indeed becomes better (middle panel in Fig. 16). Even better agreement is obtained if we use the chip-averaged dead area correction of 3.9% obtained from the analysis of the full-frame data (\*\*YOUSAF’S MEMO\*\*). In this case one expects a 2.6% difference in normalizations between the two A1795 pointings; this correction brings the two dataset in almost a perfect agreement (right panel in Fig. 16)<sup>8</sup>.

## 7 Change Log

- 4/28/04 • Herman Marshall pointed out that the MRK421 was placed at CHIPY = 177 (not at 120), so the  $\tau_L$  value for the fluffium model is revised (see §5.2)
- 5/09/04 • Extend time-dependence measurements until end of April, 2004. The points follow the previous fit, so eqs. (3–7) were not updated.

---

<sup>8</sup>*Caveat:* the CHIPY-dependence of the dead area is not observed in the full-frame data. This problem is still under investigation.

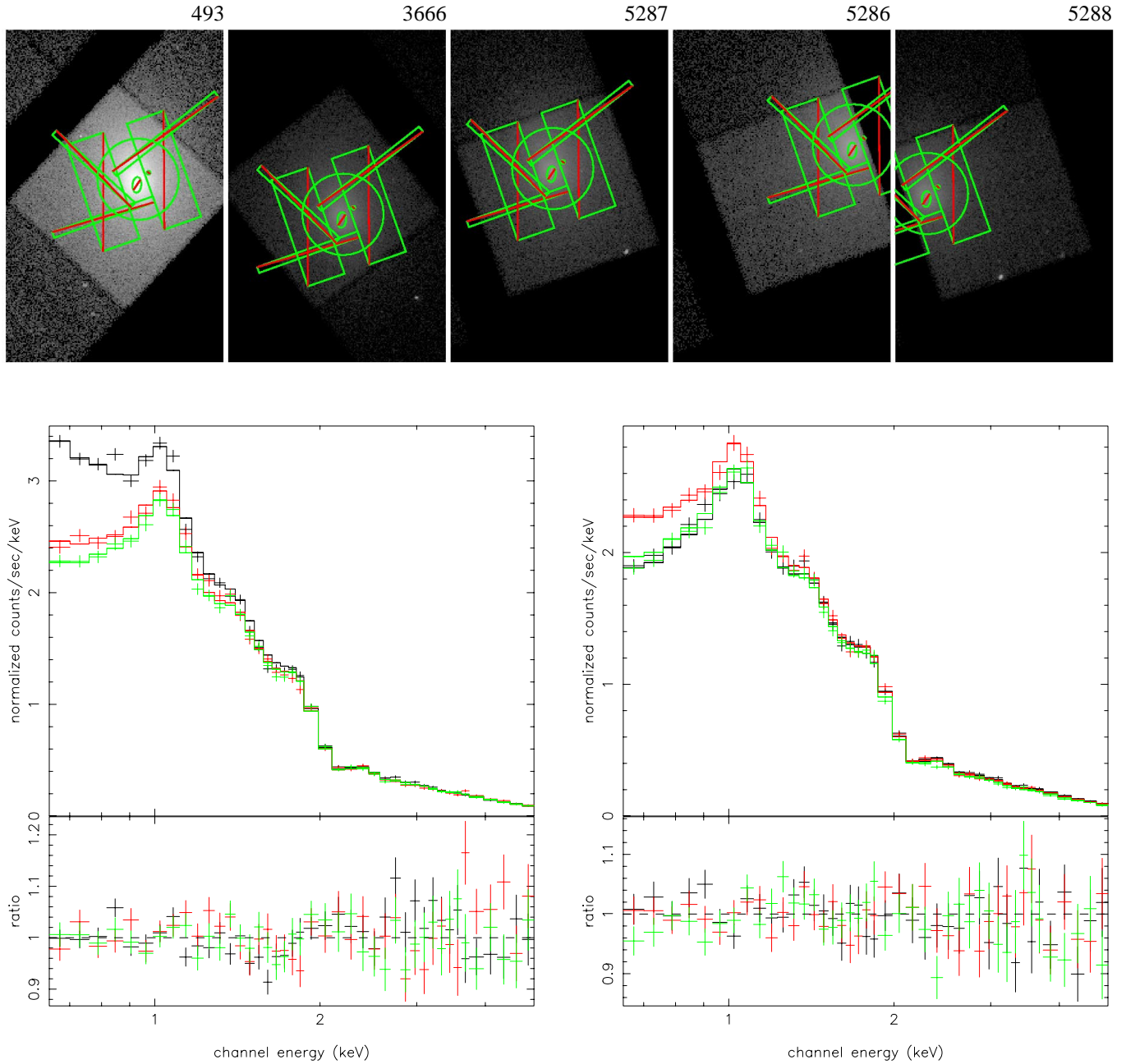


Fig. 12— Test of the **contamination spatial structure in ACIS-S**. The spectra were extracted in the  $80''$  strip and within  $2'$  of the cluster center (*top panel*). The strip is aligned with the chip boundaries in the OBSIDs 5286 and 5288. A filament of the cold gas near the cluster center was excluded because its spectrum is very different from the rest of the cluster and it is attenuated differently in OBSIDs 5286 and 5288. The spectral variations in the rest of the region are small all the OBSIDs can be compared directly. *Bottom-Left*: the reference fit to the spectra observed at the center of S3 (OBSIDs 493, 3666, and 5287). *Bottom-Right*: the best-fit reference model applied to the 528\* series, OBSID 5286 (bottom of S3; black), 5287 (center of S3; red), and 5288 (top of S3; green).

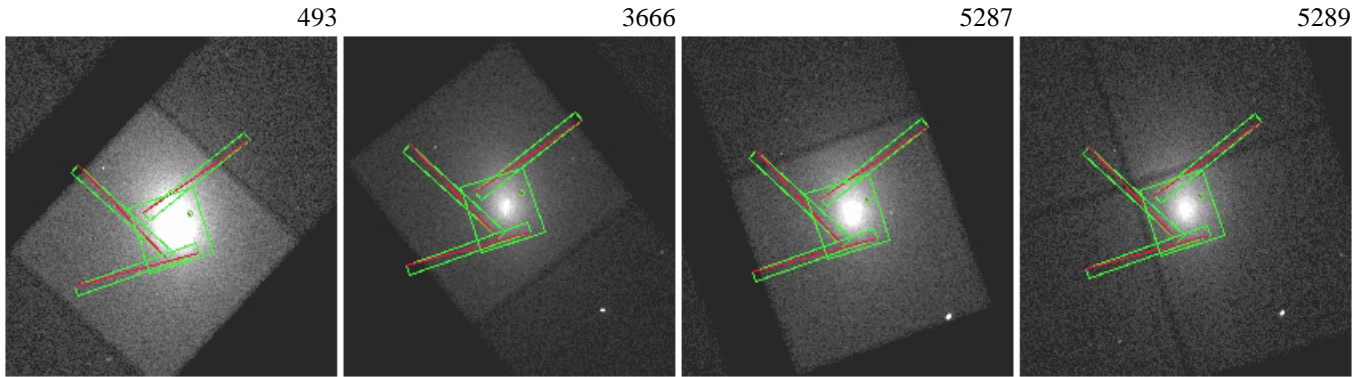


Fig. 13— The spectral extraction regions for **cross-check between the centers of ACIS-S and ACIS-I**. The spectra were extracted in  $2.6' \times 2.6'$  box aligned with the chip boundaries in the ACIS-I pointing.

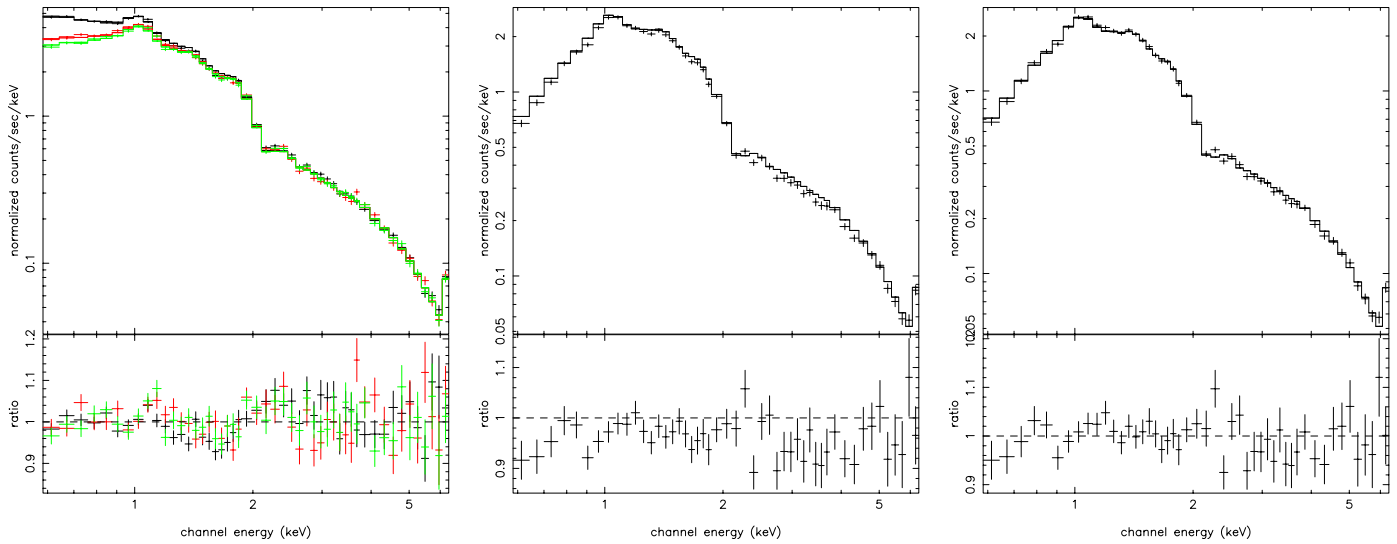


Fig. 14— Test of the **cross-calibration between the centers of ACIS-S and ACIS-I**. The spectra were extracted in regions shown in Fig. 13. *Left* — The reference model was fit to the series of ACIS-S observations (OBSIDs 493, 3666, and 5287 shown in black, red, and green, respectively). *Center* — The best fit model to the ACIS-I data applied to the ACIS-I pointing (OBSID 5289) shows systematic excess over the data, attributable to the dead area produced by cosmic rays in the FI chips. *Right* — After the *energy-independent* correction by  $(3.6 \pm 0.4)\%$ , the reference fit to the ACIS-S data agrees with the ACIS-I spectrum within 3–5% at all energies.

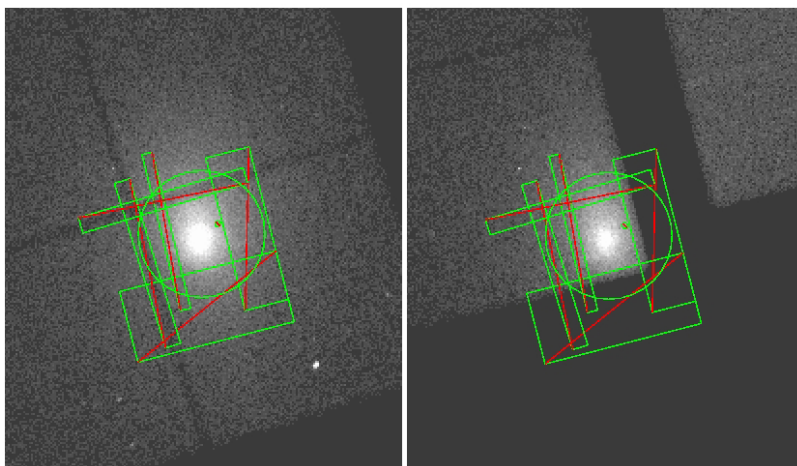


Fig. 15— The spectral extraction regions for the check of the **spatial dependence of contamination in ACIS-I**. 5289 is on the left and 5290 is on the right.

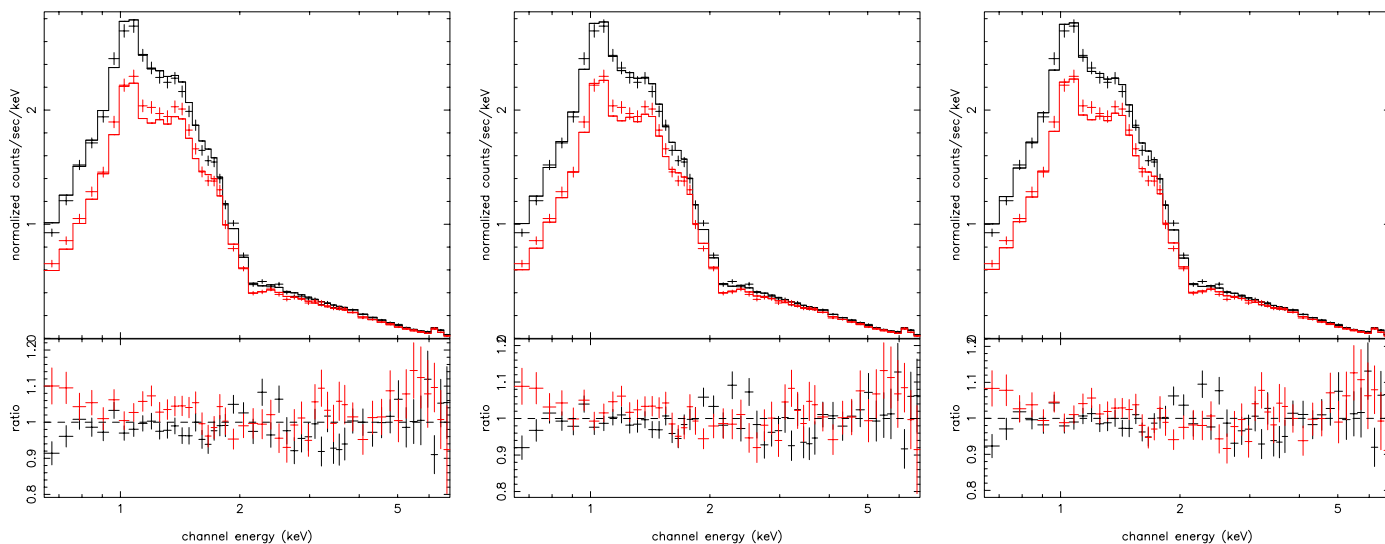


Fig. 16— Test of the **spatial dependence of contamination in ACIS-I**. The spectra were extracted in regions shown in Fig. 13. The spectra from OBSIDS 5289 (black) and 5290 (red) were fit jointly. The difference between the observed spectra is due to increased contamination at the edges of ACIS-I (major effect) and HRMA vignetting (minor effect). *Left* — model normalizations for both OBSIDS are the same. The systematic difference in the residuals is probably attributable to the CHIPY-dependence of the dead area. *Center* — the model normalization for OBSID 5290 is increased by 1.8% corresponding to the top-of-the-chip dead area correction of 3.6% derived from the A1795 data (see §6.3 and Fig. 14). *Right* — The normalization for OBSID 5290 is increased by 2.6% corresponding to the chip-averaged dead area correction of 3.9% (\*\*SEE YOUSAF’S MEMO\*\*).